https://dx.doi.org/10.1016/j.trgeo.2020.100367

Microstructural evolution of remolded clay related to creep

Dan **ZHAO**[1], Qian-Feng **GAO**[2], Mahdia **HATTAB**[3], Pierre-Yves **HICHER**[4], Zhen-Yu **YIN**[5,*],

[1] College of civil engineering and architecture, Zhejiang University of Water Resources and Electric Power, Hangzhou, China.

[2] School of Traffic & Transportation Engineering, Changsha University of Science & Technology, Changsha 410114, China.

[3] Laboratoire d'Etude des Microstructures et de Mécanique des Matériaux, Université de Lorraine, CNRS UMR 7239, Arts et Métiers ParisTech, F-57000 Metz, France

[4] Institut de Recherche en Génie Civil et Mécanique, CNRS UMR 6203, Ecole Centrale de Nantes, Université de Nantes, France.

[5] Department of Civil and Environmental Engineering, The Hong Kong Polytechnic University, Hung Hom, Kowloon, Hong Kong, China.

[*] Corresponding author: Dr Zhen-Yu YIN, Tel: +852 3400 8470; Fax: +852 2334 6389; E-mail: zhenyu.yin@polyu.edu.hk; zhenyu.yin@gmail.com

Abstract: The aim of this study is to understand the local mechanisms related to creep behavior of a typical clay under triaxial loading. The investigation concerns both normally consolidated and overconsolidated specimens of remolded kaolin clay. The macroscopic results showed that both dilatancy and contractancy could occur during creep depending mainly on the clay behavior prior to the creep test. The magnitude of the dilatancy/contractancy was controlled by the stress level, on one hand, and by the overconsolidation ratio which governed the sign of the volumetric strain variation during triaxial loading, on the other hand. At the microscopic scale, the dilatancy/contractancy phenomena were analyzed using the scanning electron microscopy (SEM). The results indicated that the microstructural evolution of the clay along mechanical loading depended on the stress history. The structural evolution during the creep phases followed the structural pattern developed under monotonic loading. The creep dilatancy phenomenon appeared strongly related to the expansion of micro pores and micro cracks within the overconsolidated clay specimens.

Key words: Remolded Clays; Overconsolidation ratio; Dilatancy; Creep; Triaxial test; Microstructure

1. Introduction

Clay exhibits time-dependent deformations under sustained loads, which is known as creep (i.e. Singh & Mitchell, 1968; Bishop & Lovenburry, 1969; Mesri & Goldewski, 1977; Vaid & Campanella, 1977; Tavenas et al., 1978; Leroueil et al., 1985; Yin and Hicher, 2008; Yin et al., 2010, 2011; Hicher, 2016; Zhu et al. 2016; Yin et al. 2017). According to the strain rate, the process of creep is usually divided into three phases: (i) primary creep or transient creep, (ii) secondary creep or steady creep, and (iii) tertiary creep or acceleration creep. The creep in clay can result in excessive deformations, and thus may cause various geotechnical problems associated with clayey soils, such as foundation and embankment settlements, instability of earth-retaining structures, and slope failures (i.e. Tavenas & Leroueil, 1980; Rowe & Hinchberger, 1988; O'Reilly et al., 1991; Karstunen andYin, 2010; Yin et al., 2015). This has raised a great need to study the creep behavior of clay.

Many experimental results obtained on clays under constant loads in oedometric and triaxial testing systems have been reported. For instance, Tian et al. (1994) carried out drained triaxial creep tests on normally consolidated undisturbed marine sediments. Their results showed that the variations of both axial strain and axial strain rate with time could be characterized by power law functions and the magnitude of the axial creep strain depended on the stress level. However, the development of volumetric deformations during creep has received less attention. Sekiguchi (1973) performed drained triaxial creep tests which showed that contractive creep gradually developed in a normally consolidated remolded clay and that the variation of the volumetric creep strain was dependent on the effective stress ratio ($\eta = q/p'$, where q is the deviatoric stress and p' is the mean effective stress). Tavenas et al. (1978) conducted drained and undrained triaxial creep tests on lightly overconsolidated intact Saint-Alban clay along different stress paths. The authors stated that a contractive creep occurred along the p'-increased stress path, little volume change occurred along the constant p' stress path, and a clear dilative creep developed along the p'-reduced stress path, indicating that the volumetric creep deformation was stress path-dependent. Drained triaxial creep tests performed on undisturbed marine sediments by Tian et al. (1994) also showed that the volumetric creep strain remained small and the strain rate decreased with time at a low stress level. At a high stress level, large volumetric creep deformation initially developed with high strain rate, this phenomenon being followed by a rapid reduction in strain rate. Along undrained triaxial creep tests on a stiff natural clay, Yano et al. (1997) reported that dilatancy occurred not only during the shearing process but also during the creep process for a dilative material. Zhao et al. (2019) examined the creep behavior of clay through drained triaxial creep tests along purely deviatoric stress paths. The authors showed that the loading history had a significant influence on the amount of dilatancy during creep. The above results suggest that the complex creep-dilatancy behavior of clay still needs a clearer understanding; the central point could be how to approach the microscopic origin of such phenomenon.

Previous studies have provided evidences that the macroscopic behavior of clayey soils is mostly determined by its microstructural state (Hicher et al., 2000; Hattab et al. 2010; Hattab and Favre, 2010; Hammad et al., 2013; Xie et al., 2018; Gao et al., 2020). Thus, an investigation of the clay microstructure may help bringing new insight into the creep-dilatancy phenomenon. To date, the clay microstructure has been analyzed by many researchers (for example Diamond, 1971; Delage & Lefebvre, 1984; Bai & Smart, 1997; Hicher et al., 2000; Hattab & Fleureau, 2010; Gao et al., 2020). These studies imply the identification of clay properties at the microscopic level including the arrangement and distribution of particles, aggregates and pores, as well as their contact and connectivity under different stress conditions. The different techniques for microstructure observations consist mainly on the mercury intrusion porosimetry (MIP), the scanning electron microscopy (SEM), the transmission electron microscopy (TEM), the X-ray micro tomography (XR-μCT), etc. For instance, Hicher et al. (2000) and Hattab and Fleureau (2010) performed triaxial tests followed by SEM observations on remolded saturated kaolin clays and highlighted the relation between the loading paths and the local mechanisms. Based on the work of Hattab and Fleureau (2010, 2011) and Gao et al. (2020) proposed five conceptual modes of particle orientation and further linked the dilatancy phenomenon to the tortuous arrangement of clay particles and the development of mesoscale cracks during triaxial loading. Concerning the creep behavior, Pusch (1979) stated that the processes involved in the creep of clay are also strongly dependent on the microstructure. Li et al. (2010) studied the creep characteristics and microscopic pore variation of soft soil under different drainage conditions. They reported that the gradual change in the micropore properties revealed the micro-mechanism of soft soil creep. Wang and Wong (2016, 2017) performed drained triaxial creep tests on a saturated till and an oil sand. The authors considered that the inelastic strain developed during creep corresponded to irreversible rolling between grains over time. The microstructure of geomaterials can be quantitatively represented by its inelastic strain. Xie et al. (2018) investigated the microstructure of a loess-like soil after triaxial creep tests using the SEM technique. The authors stated that the creep was closely related to the orientation of particles and pores, as well as the interconnection of pores. They also revealed that the evolution of the meso-pores was the most important factor leading to the creep of loess-like soils. Nevertheless, this aspect is still under discussion and a better understanding on the creep-dilatancy mechanism in clays from the microscopic point of view is needed.

The objective of this study was to try to understand the physical origin of the creep-dilatancy phenomenon in clay. The experimental approach consisted in performing triaxial creep tests, on both normally consolidated and overconsolidated remolded clay samples, considering different loading conditions. On this basis, the time-dependent behavior, particularly the evolution of the volumetric creep strains, in remolded clay was deeply analyzed. The microstructural characteristics including particle orientations and pore properties (pore shape and orientation), before and after the creep stage tests, were subsequently quantified using the SEM technique. Finally, the local mechanisms explaining the creep-dilatancy in clay were revealed by linking the microstructural characteristics to the mechanical behavior.

2. Material and experimental techniques

2.1 Material properties

The material selected for this study is an industrial clay termed Kaolin K13 (Sibelco, France). The liquid limit is 42% and the plastic limit is 21%. The pycnometer tests suggested that the specific gravity of the material is 2.63. Oedometer tests showed that the compression and the swelling index are $C_c = 0.28$ and $C_s = 0.09$, respectively. The physical and mechanical properties of Kaolin K13 clay are listed in Table 1. Fig. 1 presents the grain size distribution of the raw clay powder obtained by the laser granulometry. It shows that approximately 60% of the grains are smaller than 9 μm, which corresponds more to the aggregates sizes rather than the unit kaolinite particles.

2.2 Procedure for ~~T~~triaxial creep tests

A clay slurry with an initial water content of $1.5w_L$ was prepared by mixing the Kaolin K13 powder with a certain amount of de-aired water. After curing for 48 h, the clay slurry was deposited in a double-drained cylindrical consolidometer for one-dimensional consolidation. Then, a maximum effective stress of 120 kPa was applied to the clay slurry in several steps, and the whole consolidation process lasted for three weeks. Afterwards, the clay core was gently trimmed into cylindrical specimens of 75 mm in height and 50 mm in diameter for triaxial testing.

Triaxial creep tests were carried out on saturated remolded kaolin specimens using the GDS triaxial testing system. The temperature of the laboratory was always maintained at 20°C to eliminate the influence of temperature change on the test results. In this study, the triaxial creep test was conducted following these steps:

- *Saturation*: Skempton's pore pressure parameter $B = \Delta u/\Delta\sigma_3$ approached 100%

- *Isotropic consolidation*: the consolidation pressure p'_{0i} was applied up to 1000 kPa for normally consolidated conditions, and $p'_i = p'_{0i}$/OCR for overconsolidated conditions.

- *Triaxial shearing*: purely deviatoric stress paths were applied with a loading velocity of 0.0025 mm/min.

- *Creep test*. When the desired stress level was achieved, both p' and q were kept constant; thereafter, the creep test started. The evolution of the volumetric creep strain was measured every three minutes by the GDS data acquisition system.

For further details on the test procedure, the reader can refer to Zhao et al. (2019). The specification of the triaxial tests, divided into two categories, is summarized in Table 2. The specimen denomination corresponds to the loading condition; for example P_{010}-OCR1.5-q200, P_{010} represents the specimens consolidated here under p'_{0i} = 1000 kPa; OCR1.5 represents the specimens with OCR equal 1.5 (the NC symbol represents normally consolidated specimens); q200 indicates that a deviatoric stresses of 200 kPa was applied during creep.

After triaxial testing, all the specimens were unloaded by steps collected and sealed within film paper, tin foil and paraffin. They were afterwards kept at room temperature.

2.3 Microstructural observations

2.3.1 Specimens and observations

The core zone of each specimen was cut into a soil board. Then, a parallelepiped sub-specimen with the dimension of 10 mm × 30 mm × 10 mm and a cubic sub-specimen with the side length of 10 mm were extracted from the soil board with a blade (Fig. 2a). Note that the length direction of the parallelepiped sub-specimen was perpendicular to the axial stress (σ'_1) applied in triaxial creep tests. Afterwards, all sub-specimens were dehydrated using the freeze-drying method which is a good choice particularly for kaolin clay without disturbing the fabric (Hattab et al., 2010 & 2015). The fresh planes used for SEM observation were obtained by fracturing the parallelepiped sub-samples in the middle cross sections at the freezing stage of the freeze-drying process (Gao et al., 2020).

Prior to SEM observations, the fresh cross sections of the sub-specimens were vacuum coated with thin layers of gold to inhibit electrostatic charge and reduce thermal damage. The gold metallisation was carried out using the Cressington 108 auto sputter coater, at 30 mA and 15 mbar for 20 s. The prepared SEM sub-specimens were mounted on a sample holder and observed using the JEOL Model JSM-6490 microscope at an accelerating voltage of 10 k and a working distance of 10 mm. Since an SEM image gives only the information at a local point, a large number of images are required to make a reasonable statistical interpretation. Previous studies, among them Hattab et al. (2010), Zhang and Cui (2017) and more recently Gao et al. (2020), have showed that the SEM images with magnifications of 1000× up to 5000× are all suitable for the identification of the clay microstructure. Thus, a 3000× magnified image was saved at each point. On the other hand, by comparing two different methods of treatment, automatic method and semi-automatic method, Gao et al. (2020) showed that a global orientation curve deduced from 10 representative ×3000 magnified images, containing approximately 5000 particles, was quite sufficient to identify with good accuracy the microstructure properties of the kaolin clay. Thus, in this work, 20 points were selected randomly in the cross section of each sub-specimen for imaging (Fig. 2b), which represent at least 8000 counted kaolinite particles.

2.3.2 Image processing method

Kaolinite particles are rigid platelets which can be considered as ellipse flakes, especially in the vertical plane of a specimen (Fig. 3a). Thus, Using the Photoshop software, the particles were manually marked one by one by lines having the same length and orientation as the particles (Fig. 3b), as proposed by Hattab et al. (2010). Thereafter, the orientations of the fitted lines of particles could be measured by a free access software named Image J. The orientations of all the represented particles with respect to the X-axis (perpendicular to the axial stress) can thus be calculated. The advantage of this semi-automated method for the identification of clay particles has been presented in Gao et al. (2020). The imaging plane was divided into a given number of quadrants, each of them equal to 15˚ referring to the work of Hicher et al. (2000), Hattab & Fleureau (2010) and Gao (2020). The number of particles oriented towards each quadrant was counted and thus the percentage of particles towards each quadrant was calculated. The orientations of the particles of a specimen can be represented by two methods, the rose diagram representation (see Fig. 3c) or the orientation curve as presented in Fig. 3d. In the latter representation the D line, with a mean percentage of 8.3%, represents a perfectly isotropic microstructure (Hattab & Fleureau, 2011).

On the SEM images, one can observe that pores and particles are distinguished through zones of different gray levels. Pore properties (orientation and mean diameter) can be identified by the image processing technique. Fig. 4 presents the main process for the identification of pore spaces by means of the ImageJ software. The original image was transformed into the binary image by setting an optimal threshold value (Fig. 4a-c). in which the particles/pores are shown in white/black. Since the threshold determines the accuracy of the image processing, the threshold operation was made several times for each image and the average value was used in the final analysis. Local particular black parts identified falsely as pores by the software ImageJ, such as the projections of particle aggregates in zone A and B (Fig. 4), were removed manually from the binary image (Fig. 4c).

Note that in the binary image, many connected pores were identified as single pores. To address this problem, the watershed algorithm was applied to the binary image (Fig. 4d). In this way, the connected pores could be reasonably separated. Finally, each isolated pore was replaced with an ellipse of identical area, orientation and centroid (Fig. 4e). The area of a single pixel in each SEM image was 0.001 μm^2. To avoid processing errors, only those pores with areas larger than 0.05 μm^2 were identified. Through this process, basic geometric parameters of pores were measured.

2.3.3 Microstructural quantification

The anisotropy of the particles (or of the pore orientations) could be quantified by the orientation index according to Hicher et al. (2000) using the following expression:

$$I_{\mathrm{or}} = \frac{k + l + m}{r + s + t} \tag{1}$$

I_{or} is the orientation index, which varies from 1 (for an isotropic particle arrangement) to 0 (for a totally anisotropic particle arrangement); *s* is the maximum percentage in the rose diagram (Fig. 5a); *r* and *t* are the percentages of the two zones beside the maximum frequency zone; *k*, *l*, *m* are the percentages of the zones perpendicular to the zones *r*, *s* and *t*, respectively.

The shape of a pore can be characterized by the pore roundness, expressed by:

$$R_s = \frac{B}{A} \tag{2}$$

R_s is the pore roundness, which approaches 0 for a very elongated pore, and 1 for an equiaxed pore (see Fig. 5b); *A* is the major axis length of the fitted ellipse; *B* is the minor axis length of the fitted ellipse.

Based on SEM images, the microporosity and micro-void ratio could be calculated by:

$$n_s = \frac{A_p}{A} \tag{3}$$

$$e_s = \frac{n}{1 - n} \tag{4}$$

n_s is the microporosity obtained from the analysis of SEM images; A_p is the total areas of pores; *A* is the area of the image; e_s is the micro-void ratio obtained from the analysis of SEM images.

3. Mechanical behavior of kaolin clay along p' constant stress path and creep phenomenon

3.1 Mechanical behavior during monotonic loading

Fig. 6 shows the results of 6 specimens subjected to triaxial loading till a given stress level, along the purely deviatoric stress path. These results have already been deeply analysed and discussed in Zhao et al. (2019). In Fig.6c one can observe the evolution of the volumetric strain as a function of the axial strain in the plane (ε_1-ε_v), exhibiting different tendencies depending on stress conditions. For normally consolidated and lightly overconsolidated specimens (OCR<2.5), a contractancy was obtained corresponding to a decrease of the void ratio towards the critical state line in the *e-log p'* plane (Fig. 6d). For highly overconsolidated samples, a dilatancy was observed accompanied by an increase in the void ratio heading also to the critical state in the *e-log p'* plane. For all overconsolidated samples, no volumetric strain variation was observed at the first stages of the triaxial loading (Fig. 6c). Moreover, quite consistent curves were obtained for tests with the same OCR and greater deformation was developed under higher stress levels (e.g., test P_{010}-NC-q200 and P_{010}-NC-q670). Notice that the same tendency was observed in the results of the 6 shear tests.

The mechanical behavior identified here on Kaolin K13 is well consistent with that identified by Ighil Ameur (2016) and Gao et al. (2020) on the same material showing the influence of the stress path on the macro and micro behavior. These results are also quite well consistent with previous results on different clays along constant p' loading triaxial tests, as for example in the works of Shimizu (1982) on Fujinanori clay and Hattab and Hicher (2004) on Kaolin P300.

3.2 Creep behavior after monotonic loading

After the monotonic loading on purely deviatoric stress paths, the 6 specimens were carefully sealed for micro observation.

For the 6 other specimens of the creep group, after the stress deviator q was loaded up to the target value in a single stage, both p' and q were maintained constant; thereafter, the pure creep phase began. Fig. 7 presents the stress conditions during this phase in the (p'-q) plane. In this plane, the contractancy, dilatancy and no-volume change domains identified by Hattab and Hicher (2004) were superimposed. The authors demonstrated that the no-volume change zone identified along the first stages of purely deviatoric stress paths corresponds to the pseudo-elastic volumetric domain highlighted earlier by Biarez and Hicher (1994) for constant σ'_3 drained triaxial tests.

The evolutions of the volumetric creep strain ($\varepsilon_{v\text{-}creep}$) as a function of time (t_{creep}) are presented in Fig. 8. The creep deformation is more pronounced for normally consolidated samples within the contractancy domain, as well as for highly overconsolidated specimens within the dilatancy domain. The results of the creep phase highlighted that the deformation tendency was the same as the one obtained under purely deviatoric stress loading. The evolution of $\varepsilon_{v\text{-}creep}$ under a purely deviatoric stress path for normally consolidated kaolin clay is consistent with that under constant σ'_3 by Tian et al (1994) and under an increasing p' stress path by Tavenas et al. (1978) and Sekiguchi (1973).

For lightly overconsolidated samples located in the no-volume change (the pseudo-elastic volumetric) domain, the results showed that a volumetric strain evolution alternating between very small contractancy/dilatancy and dilatancy/contractancy occurred. These results seem to be directly related to the stress control conditions where the stress level needs to be maintained. Considering the very slight volumetric strain variations obtained here, we can assume that no-volumetric strain related to creep develops within the no volume change domain.

Finally, the results at the macro scale showed that the strain evolution during creep followed the same trend as during the initial loading stages.

After the creep tests, the 6 samples were carefully sealed for observations at the micro scale.

4. Microstructural behavior of clay related to creep

The study of the kaolin clay microstructure is based on the study of the arrangement of solid particles, as well as the pore properties. In this respect, after each mechanical test (shear only on the one hand, and shear + creep on the other hand), the evolution of the particle orientation and the pore properties related to different stress states and loading histories were examined. The analysis focused mainly on the 3 representative groups of normally consolidated samples (P_{010}-NC-q200) within the contractancy domain, lightly overconsolidated samples (P_{010}-OCR2.5-q200) within the pseudo-elastic domain, and highly overconsolidated samples (P_{010}-OCR4-q200) within the dilatancy domain. For all these tests, the creep stage was performed at the same deviatoric stress level q = 200 kPa within these three domains, as presented in Fig. 7.

4.1 Analysis of clay particle orientation

4.1.1 Within the contractancy domain for normally consolidated specimens

In the contractancy domain, the soil was contractant along the constant p' stress path. This contraction continues to develop during the creep stage, as it can be observed at the macroscale in Fig. 8. Fig. 9 shows the normally consolidated specimen P_{010}-NC-q200, the path being conducted up to q = 200 kPa within the contractancy domain. The strain evolutions for samples, (P_{010}-NC-q200) $_{shear}$ and (P_{010}-NC-q200) $_{creep}$, are highly consistent during the monotonic loading phase (Fig. 9b), which permits to directly identify the evolution mechanisms related to creep. Following the experimental procedure described in *section 2.3.2*, the microstructural organisation could be identified through a rose diagram (Fig. 10a) or orientation curve (Fig. 10b). The orientation 0° here represents the plane perpendicular to the major principal effective stress σ'_1. The ***D*** line means perfect isotropic orientation as defined by Hattab & Fleureau (2010).

In Fig. 10a and Fig. 10b the results of 14 photos including 7227 particles of the sample after creep (P_{010}-NC-q200)$_{creep}$, 10 photos with 4347 particles from the sample (P_{010}-NC-q200)$_{shear}$ after monotonic loading are presented. The analyses combining all the treated images, presented here with two different representations, show that the kaolinite particles are mainly oriented in a preferential direction from 150° to 165°, depending on the test conditions. This induced anisotropy could be observed in both tests. Under monotonic loading the results appear in agreement with those obtained by Gao et al. (2020). During creep, the anisotropy was activated continuously, resulting in more clay particles oriented in the same direction of about 165°. It can be seen very clearly that a higher peak value appeared after creep (point **P** in Fig. 10b). Thus more individualized particles reoriented in the direction of about 165°. Furthermore, by changing from 0.06 for (P_{010}-NC-q200)$_{shear}$ to 0,02 for (P_{010}-NC-q200)$_{creep}$, the I_{or} parameter value showed a more marked anisotropy after the creep stage.

The orientation curves are equivalent to the rose diagram representation, but they highlight more phenomena regarding the microstructure state. Therefore, in the following analyses, the orientation curves will be preferably used to illustrate the global particle orientation.

Fig. 11 presents representative SEM photos of tests P_{010}-NC-q200 within the contractancy domain after shear and after creep, where the red dotted lines indicate examples of particle groups giving the microfabric-oriented information. These images illustrate how particles oriented themselves during the mechanical loadings. The particles are mostly arranged face-face along oriented planes, and more particles are oriented along the same planes after the creep stage (Fig. 11b) than after the monotonic shear loading (Fig. 11a). The microstructure reorientation progressed during creep resulting in more stable face-face contacts, accompanied with a denser structure and, at the global scale, a decrease of the void ratio during creep contractancy.

4.1.2 Within the pseudo-elastic domain

For lightly overconsolidated specimen within the pseudo-elastic domain, very limited volumetric strain developed under constant p' stress loading path. At the macroscopic scale, no volumetric creep strain is assumed to develop, as explained in Section 3.2, as well as by Zhao et al. (2019). Fig. 12 shows the stress condition and the strain evolution of the lightly overconsolidated specimens (P_{010}-OCR2.5-q200).

A quantitative analysis of the particle orientation through SEM images is shown in Fig. 13. The preferential orientation of the clay particles is in the 150° to 165° interval for both samples, one representing the microstructure after the triaxial shear, the other after the triaxial shear + creep. The material seems here to develop an anisotropic microstructure similar to that corresponding to normally consolidated specimens within the contractancy domain. Moreover, the particle orientation curves after shear and after creep are quite close. This demonstrates that a very limited structure rearrangement took place during creep.

Fig. 14 shows the example of SEM images of samples whose stress loading conditions are located within the pseudo-elastic domain. One can see that no major differences are observed in the structure state after shear and after creep. The two-slip plane pattern of particles results from the microstructural rearrangement under the constant p' stress path. Similar results were obtained for lightly overconsolidated specimens with OCR=1.5 in this pseudo-elastic domain (see the stress levels and volumetric strain variations in Fig. 7 and Fig. 8).

4.1.3 Within the dilatancy domain

At the macroscopic scale, the shear dilatancy of highly overconsolidated sample developed under monotonic loading and this dilatancy continued to develop in the pure creep stage as shown in Fig. 15.

Fig. 16 presents the percentage of particle orientation after shear and after creep. Unlike the samples located within the contractancy domain, less clear marked preferential orientations could be identified for samples in the dilatancy domain. For $(P_{010}\text{-OCR4-q200})_{shear}$, the figure shows that a large number of particles are oriented toward 160°, however the part of the orientation curve from 65° to 10° tends to approach the D line, which means that the microstructure tends towards a destructured material. This tendency becomes even more marked after the creep stage $(P_{010}\text{-OCR4-q200})_{creep}$, resulting in a line approaching even closer to the D line (Fig. 16). The representative SEM images in Fig. 17 can help explaining these results. The evolution towards structural isotropy in the creep phase is due to the rearrangement of particles in groups (see the red dotted line in Fig. 17b) forming random open micro-cracks inside the specimen (see the blue circles in Fig. 17b). Notice that this typical microstructure in the dilatancy domain develops with a softening phenomenon of the material. The next section concerning the porosity evolution will give more insights to explain this aspect of the clay behavior.

4.2 Variation of the pore properties

The geometric properties of the pores associated with the particle orientations permits us to quantify the microstructure evolution of clay related to creep. As presented in the section 2.3.2, most micropores in clay specimens have more or less an elliptical shape during triaxial loading. This makes it possible to examine the direction and shape of these micropores.

4.2.1 Pore orientation

The particles in movement during the mechanical loading tend to have a certain preferred orientation in space, and the corresponding inter-particle pore geometry gives orientation information of the structural rearrangement. Generally, and as expected, the global pore orientation under different stress conditions is quite consistent with the particle orientation identified in *Section 4.1*.

For example, a significant structural anisotropy can be observed in the normally consolidated samples in the contractancy domain (Fig. 18a). The micropores in these specimens are oriented mainly in the range from 150°-165°. The anisotropy tendency is highlighted after a certain creep time, resulting in a curve clearly farer from the isotropic D_{pore} line. The D_{pore} line (in terms of pore orientation) has a similar meaning as the depolarization line (D line) of particle orientation. A significant influence of the OCR, linked to the dilatancy mechanism, on the pore orientation could be observed. As shown in Fig. 18c, the dilative specimens $(P_{010}\text{-OCR4-q200})_{shear}$ have smaller maximum percentages; the orientation curves seem to approach the D_{pore} line, which indicates that more random micropore orientations developed within the specimens. This tendency continued to develop during the creep phase (see $(P_{010}\text{-OCR4-q200})_{creep}$ curve), resulting in numerous open micro cracks within the specimens as observed in Fig. 17b.

4.2.2 Pore shape

As illustrated in Fig.5, the pores identified in SEM images can be represented by ellipses as shown in Fig. 5. The shape characteristic of the pores can thus be evaluated through the roundness of the fitted ellipse by Eq.2, where for instance Rs =1 means circle shape of the pore.

<u>-within the contractancy domain</u>

Fig. 19 presents the statistical results of the pore shape variations in normally consolidated specimens P_{010}-NC-q200. The percentage of mean roundness before and after creep is the same

(Rs=0.45). For Rs＞0.45, the percentage of Rs in the creep sample is smaller than that in the shear sample; whereas for Rs< 0.45, an opposite tendency can be found. This means that the pores tend to be flatter after the creep stage. The variation of the pore shape is mainly due to the change in the size of the pore diameter (Fig. 19c); the mean pore diameter in the creep sample is smaller than in the shear sample, while the pore length before and after creep remains relatively unchanged (Fig. 19b). In general, the pore roundness increases with the pore diameter (Fig. 19d). It can be seen that the difference between the creep and the shear samples is mainly in the range of D>0.14 μm, indicating that the large pores are more likely to contract during creep, resulting in a denser structure, whereas small or flat pores remain unchanged.

- within the pseudo-elastic domain

For tests P_{010}-OCR2.5-q200, no volume change occurred at the macroscopic level in the creep phase (see Fig. 12b). At the microscopic level, the pore shape after creep remained mostly unchanged. The mean roundness of the pores is 0.45 and the mean pore diameter is 0.179 μm for the two samples.

- within the dilatancy domain

Fig. 20 shows the evolution of the pore shape for tests P_{010}-OCR4-q200; it appears that the mean pore roundness increased after creep (Fig. 20a). The variation of the pore shape for (P_{010}-OCR4-q200)$_{creep}$ results from the expansion in the length as well as in the diameter. For a pore length larger than 0.713 μm (Fig. 20b), the percentage of pore length in the creep sample is higher than in the shear sample. This result indicates that the large pores were likely to extend during creep, which suggests the opening of micro-cracks within the sample. This result appears consistent with the previous analyses of the variation of particle and pores orientations. Similarly, Fig. 20c shows that the percentage of large pores (D > 0.358 μm) increased after creep. It can be noted that the expansion in the pore diameter and length occurring during the creep phase tended to begin in the largest pores, as represented in Fig. 20d. For the pore diameters smaller than 0.358 μm, the percentage versus the pore diameter for creep and shear samples coincided, which means that the small pores did not contribute to the dilatancy during creep.

5. Discussions

The statistical data drawn from the SEM images indicates that the microstructure of the kaolin clay in triaxial tests depends on the stress history in the monotonic loading stage and that the tendencies observed in monotonic loading evolve continuously in the same directions in the creep stage. Under the effect of creep contraction, free water flows out of the soil element, resulting in densification and rearrangement of the soil structure. On the other hand, creep dilation consists on an increase of the randomly assembled micro-cracks initially developed during the shear path, which expanded in length as well as in diameter during creep. The microstructural evolution related to creep mechanism is discussed below in relation with the stress state.

- For normally consolidated specimens whose stress state is in the contractancy domain, the particle orientations after shear approximate the oblique line mode, as defined by Gao et al. (2020) in the same clay along constant *p′* triaxial loading. The clay particles are mainly associated face-to-face and are highly oriented by groups towards 150° to 165°. The preferential orientation of particles corresponds to the contraction of normally consolidated clay. The main orientation of the clay particles in sample (P_{010}-OCR4-q200 and q670)$_{creep}$ is also located between 150° to 165°. This can be explained by the fact that, locally in the material, more particles tend to rotate toward this direction under constant sustained stress, which represents the induced anisotropy developed during creep. The orientation of pores is associated with the rearrangement of particles or particle groups. The geometric properties of the pores show quite similar orientation tendency. Accompanied by the induced anisotropy in creep, the pore shape and space can evolve synchronously. The most frequent pore diameter is smaller under higher deviatoric stress levels during monotonic loading and the creep stage confirms this tendency. At a macroscopic level, this phenomenon corresponds to a higher magnitude of compression under a higher stress level.

- The orientation mode after shear in the pseudoelastic domain for lightly overconsolidated specimens can be characterized by particles more or less associated by groups, oriented along oblique planes, see Fig. 14a of test (P_{010}-OCR2.5-q200)$_{shear}$ for illustration. The development of this structural mode is assumed to be related to the lightly dilatancy phenomenon in monotonic loading. For sample creeping in this volumetric domain, a null volumetric change is assumed within creep phase on the macroscopic scale. At the microscopic scale, the state of particle orientation and porosity evolve less obviously in creep phase.

- A complex random orientation, in form of a special organization of particles, occurred for the highly overconsolidated specimens in the dilatancy domain. The clay microstructure was organized in tortuous and cross-oblique lines mode identified by Gao et al. (2020) along constant *p′* triaxial shearing. This phenomenon allows highlighting the microstructure mechanism of the dilatancy phenomenon. The tortuous particle groups appeared locally with the development of numerous open microcracks crossing the material in random directions. During creep, the random orientation of the micro-cracks seemed to be reinforced and the microcracks expanded in length as well as in diameter (Fig. 21). These results highlight the mechanism of dilatancy in clayey materials.

In the dilatancy domain, the viscoplastic volumetric creep strains developed with time, resulting in a macro-strain softening. When the stress level was located close to the critical state, an accumulating large dilation caused a strength reduction due to viscoplastic softening. At the microscopic scale, the micropores inside the material tended to expand, resulting in the opening of microcracks to form macrocracks (Fig. 22). These cracks could accelerate the strength decrease of the clay specimen and provoke eventually a creep collapse, as shown in Fig. 22 for the test $(P_{02}\text{-OCR5-q43})_{creep}$; more details about this test was presented in Zhao et al. (2019).

6. Conclusion

The mechanisms of the microstructure evolution in remolded clay related to creep have been investigated, mainly through 3 triaxial shear tests and 3 triaxial creep tests in different volumetric domains. SEM photos combined with adapted image processing techniques were used to identify the microstructure properties after shear and after creep. The following conclusions can be drawn:

- The structure evolution during creep depends on the structural state at the end of the monotonic loading stage. The microstructural evolution of particles and pores identified through SEM images showed results that are consistent with the tendencies at the sample scale.
- Within the contractancy domain for normally consolidated samples, an anisotropy fabric was identified and this tendency improved during creep. The larger pores were firstly compressed and their diameter decreased during creep. Meanwhile, the pore length after shear and after creep was almost the same, indicating that the sliding movements between particles could be considered almost negligible.
- Within the dilatancy domain for highly overconsolidated samples, a clear structural isotropy was formed at the end of the monotonic loading, as the consequence of assemblies of groups of particles/pores oriented in an isotropic manner. The structural isotropy continued to develop during creep, formed by more randomly distributed particle/pore groups.
- The pores in contractive specimens were generally flatter than those in dilative samples. The mean pore diameter in the creep sample was larger than in the shear sample, corresponding to dilation at the macroscopic level. The expansion of micropores together with the opening of microcracks inside the material contributed to the dilation at the specimen scale.
- Within the pseudo-elastic domain, the structure of lightly overconsolidated samples was in an intermediate state. The evolution of particles and pores after shear and after creep were very similar, which indicated that the microstructural evolution during creep in this domain was quite limited.
- Overall, the microstructural evolution of clay in the creep phase depended on the structural pattern developed in monotonic loading, which appeared to be strongly influenced by the loading history.

Acknowledgements

The support by the China Scholarship Council for the first author is gratefully acknowledged. The other financial support for this research came from the Natural Science Youth Foundation of Zhejiang

Province (Grant No.: LQ19E080021) and RIF project (Grant No.: PolyU R5037-18F) of Research Grants Council (RGC) of Hong Kong Special Administrative Region Government (HKSARG) of China.

References:

1. Bai X, Smart R. Change in microstructure of kaolin in consolidation and undrained shear. Géotechnique 1997; 47(5): 1009–1017. https://doi.org/10.1680/geot.1997.47.5.1009.
2. Biarez J, Hicher PY. Elementary mechanics of soil behaviour: saturated remoulded soils. A.A. Balkema, Rotterdam 1994.
3. Bishop AW, Lovenburry HT. Creep characteristics of two undisturbed clays. Proceedings of VII ICSMFE, Mexico City, Mexico, 1969; 29–37.
4. Diamond S. Microstructure and pore structure of impact-compacted clays. Clays and Clay Minerals 1971; 19(4): 239–249. https://doi.org/10.1346/CCMN.1971.0190405.
5. Delage P, Lefebvre G. Study of the structure of a sensitive Champlain clay and of its evolution during consolidation. Can Geotech J1984; 21(1): 21–35. https://doi.org/10.1139/t84-003.
6. Gao QF, Hattab M, Jrad M, Fleureau JM, Hicher PY. Microstructural organisation of remoulded clays in relation with dilatancy/contractancy phenomena. Acta Geotechnica 2020; 15: 223–243. https://doi.org/10.1007/s11440-019-00876-w.
7. Hammad T, Fleureau JM, Hattab M. Kaolin/montmorillonite mixtures behaviour on oedometric path and microstructural variations. European Journal of Environmental and Civil Engineering 2013; 17(9): 826–840. https://doi.org/10.1080/19648189.2013.822428.
8. Hattab M, Bouziri-Adrouche S, Fleureau JM, Évolution de la microtexture d'une matrice kaolinitique sur chemin triaxial axisymétrique. Can Geotech J 2010 ; 47(1): 34–48. https://doi.org/10.1139/T09-098.
9. Hattab M, Favre J-L. Analysis of the experimental compressibility of deep water marine sediments from the Gulf of Guinea. Marine and Petroleum Geology 2010; 27 (2): 486–499. https://doi.org/10.1016/j.marpetgeo.2009.11.004.
10. Hattab M, Fleureau JM. Experimental study of kaolin particle orientation mechanism. Géotechnique 2010; 60(5): 323–331. https://doi.org/10.1680/geot.2010.60.5.323.
11. Hattab M, Fleureau JM. Experimental analysis of kaolinite particle orientation during triaxial path. Int. J. Numer. Anal. Methods Geomech 2011; 35 (8): 947–968. https://doi.org/10.1002/nag.936.
12. Hattab M, Hammad T, Fleureau JM. Internal friction angle variation in a kaolin/montmorillonite clay mix and microstructural identification. Géotechnique 2015; 65(1): 1–11. https://doi.org/10.1680/geot.13.P.081.
13. Hattab M, Hicher PY. Dilating behavior of overconsolidated clay. Soils Found 2004; 44(4): 27–40. https://doi.org/10.3208/sandf.44.4_27.
14. Hicher PY, Wahyudi H, Tessier D. Microstructural analysis of inherent and induced anisotropy in clay. Mechanics of Cohesive-frictional Materials: An International Journal on Experiments, Modelling and Computation of Materials and Structures 2000; 5(5): 341–371. https://doi.org/10.1002/1099-1484(200007)5:5<341::AID-CFM99>3.0.CO;2-C.
15. Hicher PY. Experimental study of viscoplastic mechanisms in clay under complex loading. Géotechnique 2016; 66(8): 661–669. https://doi.org/10.1680/jgeot.15.P.203.

16. Ighil Ameur L, Robin G, Hattab M. Elastic properties in a clayey material under mechanical loading–an estimation through ultrasonic propagations. European Journal of Environmental and Civil Engineering 2016; 20(9): 1127–1146. https://doi.org/10.1080/19648189.2015.1090926.

17. Karstunen M, Yin ZY. Modelling time-dependent behaviour of Murro test embankment. Géotechnique 2010; 60(10): 735–749. https://doi.org/10.1680/geot.8.P.027.

18. Leroueil S, Kabbaj M, Tavenas F, Bouchard, R. Stress-strain-strain rate relation for the compressibility of sensitive natural clays. Géotechnique 1985; 35(2): 159–180. http://dx.doi.org/10.1680/geot.1985.35.2.159.

19. Li JX, Wang CM, Zhang XW. Soft soil creep characteristics under different drainage conditions and micropore changes. Rock and Soil Mechanics 2010; 31(11): 3493–3498. (In Chinese)

20. Mesri G, Goldewski PM. Time and stress-compressibility interrelationship. J Geotech Engng 1977, 103: 5, 417–430. https://doi.org/10.1016/0148-9062(77)91005-1.

21. O'Reilly MP, Mair RJ, Alderman GH. Long-term settlements over tunnels: an eleven-year study at Grimsby. In: Tunnelling 91: 6th International Symposium, 1991; 4: 55–64.

22. Pusch R. Creep mechanisms in clay. Mechanisms of Deformation & Fracture 1979; 351–359. https://doi.org/10.1016/B978-0-08-024258-3.50038-2.

23. Rowe R, Hinchberger SD. The significance of rate effects in modelling the Sackville test embankment. Can Geotech J 1998; 35: 500–516. https://doi.org/10.1139/t98-021.

24. Sekiguchi H. Flow characteristics of clays. Soils and Foundations 1973; 13(1): 45–60. https://doi.org/10.3208/sandf1972.13.45.

25. Shimizu M. Effect of overconsolidation on dilatancy of a cohesive soil. Soils Found 1982; 22(4):121–133.

26. Singh A, Mitchell JK. General stress-strain-time function for soils. J Soil Mech Found Div, 1968; 94(1):19–46.

27. Tavenas F, Leroueil S, Rochelle PL, Roy M. Creep behaviour of an undisturbed lightly overconsolidated clay. Can Geotech J 1978; 15(3): 402–423. https://doi.org/10.1139/t78-037.

28. Tavenas F, Leroueil S. Creep and failure of slopes in clays. Can Geotech J 1981; 18(1): 106–120. https://doi.org/10.1139/t81-010.

29. Tian WM, Silva AJ, Veyera GE, Sadd MH. Drained creep of undisturbed cohesive marine sediments. Can Geotech J 1994; 31(6): 841–855. https://doi.org/10.1139/t94-101.

30. Vaid YP, Campanella RG. Time-dependent behavior of undisturbed clay. J Geotech Engng 1977; 103(7):693–709.

31. Wang Z, Wong RCK. Strain-dependent and stress-dependent creep model for a till subject to triaxial compression. Int. J. Geomech. 2016; 16(3): 04015084.

32. Wang Z, Wong RCK. Strain-dependent creep behavior of Athabasca oil sand in triaxial compression. Int. J. Geomech. 2017; 17(1): 04016027.

33. Xie X, Qi S, Zhao F, Wang D. Creep behavior and the microstructural evolution of loess-like soil from Xi'an area, China. Engineering Geology 2018; 236: 43–59. https://doi.org/10.1016/j.enggeo.2017.11.003.

34. Yano K, Suzuki M, Nakai T. Undrained shear and creep behavior of staff natural clay. In Proc. of Int. Symp. on Deformation and Progressive Failure in Geomechanics, IS-Nagoya, 1997; 97: 205–210.

35. Yin ZY, Hicher PY. Identifying parameters controlling soil delayed behaviour from laboratory and in situ pressuremeter testing. Int. J. Numer. Anal. Methods Geomech 2008; 32(12): 1515–1535. https://doi.org/10.1002/nag.684.

36. Yin ZY, Chang CS, Karstunen M, Hicher PY. An anisotropic elastic viscoplastic model for soft clays. Int J Solids Struct 2010; 47(5): 665–677. https://doi.org/10.1016/j.ijsolstr.2009.11.004.

37. Yin ZY, Karstunen M, Chang CS, Koskinen M, Lojander M. Modeling time-dependent behavior of soft sensitive clay. J. Geotech. Geoenviron. Eng. ASCE 2011; 137(11): 1103–1113. https://doi.org/10.1061/(ASCE)GT.1943-5606.0000527.

38. Yin ZY, Xu Q, Yu C. Elastic viscoplastic modeling for natural soft clays considering nonlinear creep. Int. J. Geomech. ASCE 2015; 15(5): A6014001. https://doi.org/10.1061/(ASCE)GM.1943-5622.0000284.

39. Yin ZY, Zhu QY, Zhang DM. Comparison of two creep degradation modeling approaches for soft structured soils. Acta Geotech 2017; 12(6): 1395–1413. https://doi.org/10.1007/s11440-017-0556-y.

40. Zhang ZL, Cui ZD. Analysis of microscopic pore structures of the silty clay before and after freezing-thawing under the subway vibration loading. Environ Earth Sci 2017; 76 (15): 528. https://doi.org/10.1007/s12665-017-6879-z.

41. Zhao D, Hattab M, Yin ZY, Hicher PY. Dilative behavior of kaolinite under drained creep condition. Acta Geotech 2019;14(4): 1003–1019. https://doi.org/10.1007/s11440-018-0686-x.

42. Zhu QY, Yin ZY, Hicher PY, Shen SL. Nonlinearity of one-dimensional creep characteristics of soft clays. Acta Geotech 2016; 11(4): 887–900. https://doi.org/10.1007/s11440-015-0411-y.

TABLES

Table 1 Physical and mechanical properties of Kaolin K13 clay

Liquid limit w_L (%)	Plastic limit w_P (%)	Plasticity index I_P	Specific gravity G_s	Compression index C_c	Swelling index C_s
42	21	21	2.63	0.28	0.09

Table 2 Drained triaxial tests on Kaolin K13 clay

Specimen	p'_{010} (kPa)	p'_i (kPa)	q (kPa)	OCR
$(P_{010}$-NC-q670$)_{shear}$	1000	1000	670	1
$(P_{010}$-NC-q200$)_{shear}$		1000	200	1
$(P_{010}$-OCR1.5-q445$)_{shear}$		666	445	1.5
$(P_{010}$-OCR1.5-q200$)_{shear}$		666	200	1.5
$(P_{010}$-OCR2.5-q200$)_{shear}$		400	200	2.5
$(P_{010}$-OCR4-q200$)_{shear}$		250	200	4
$(P_{010}$-NC-q670$)_{creep}$	1000	1000	670	1
$(P_{010}$-NC-q200$)_{creep}$		1000	200	1
$(P_{010}$-OCR1.5-q445$)_{creep}$		666	445	1.5
$(P_{010}$-OCR1.5-q200$)_{creep}$		666	200	1.5
$(P_{010}$-OCR2.5-q200$)_{creep}$		400	200	2.5
$(P_{010}$-OCR4-q200$)_{creep}$		250	200	4

Figure

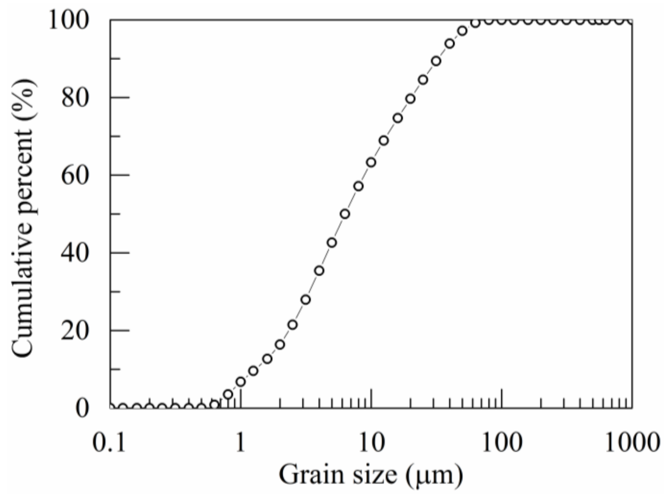

Fig. 1 Grain size distribution curve of Kaolin K13 clay

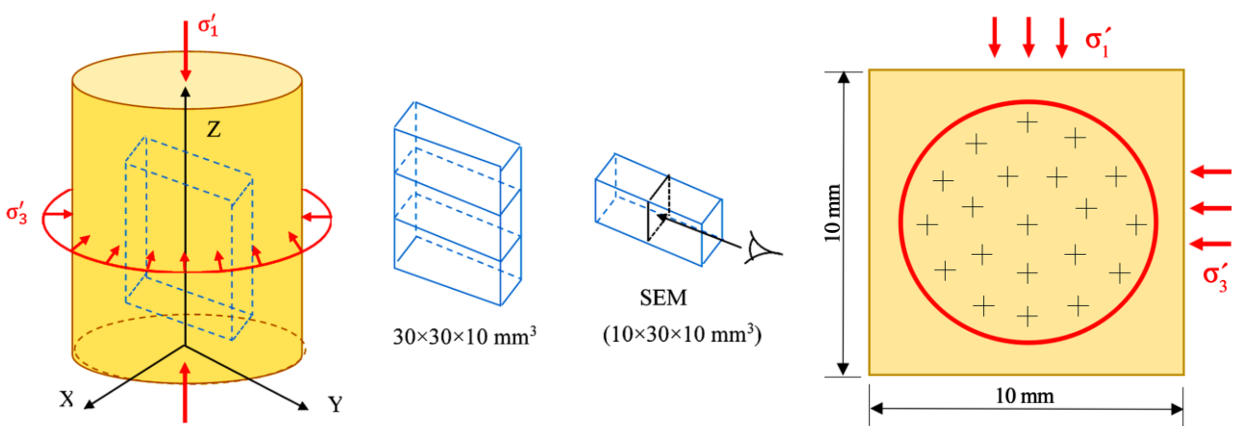

Fig. 2 Sub-specimen preparation for microscopic observations

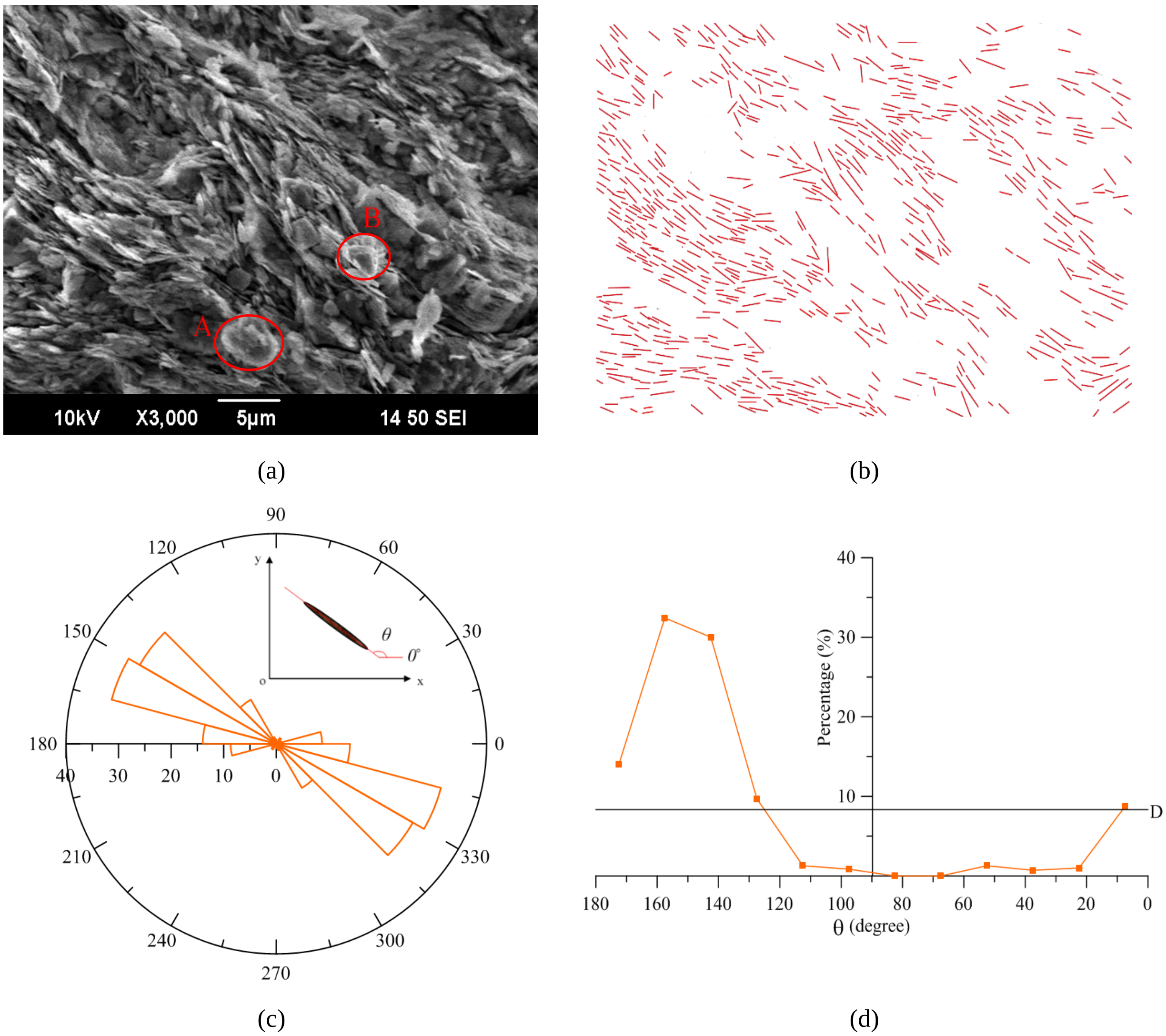

Fig. 3 Identification of particle orientation: (a) SEM image; (b) particle representation; (c) rose diagram; (d) orientation curve

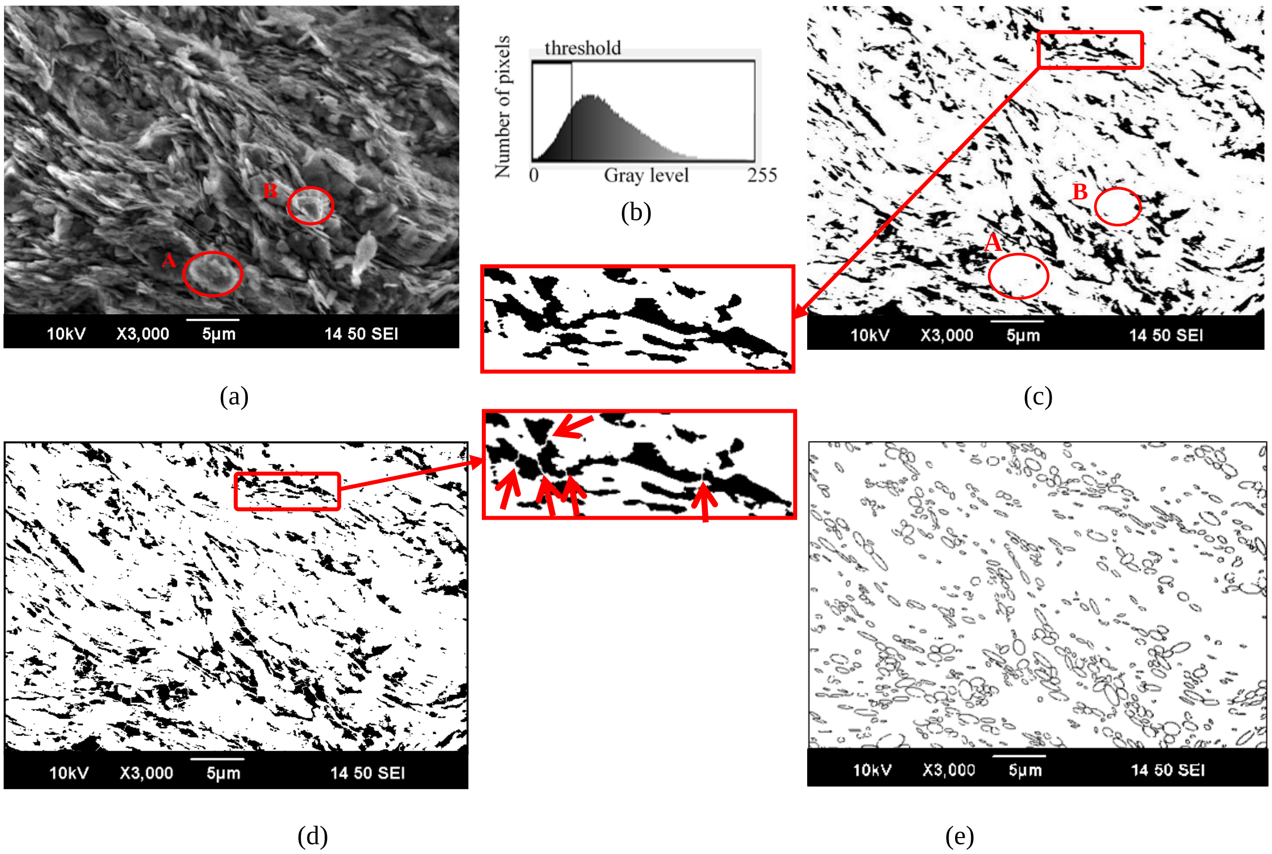

Fig. 4 Methods for the identification of pore parameters: (a) original image (b) gray level histogram (c) binary image (d) segmented image (e) ellipses image

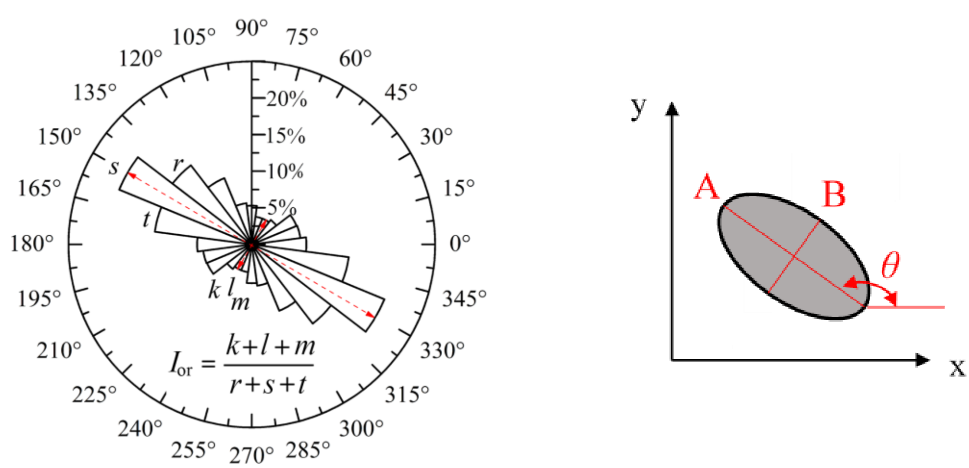

(a) Definition of the orientation index in a rose diagram

(b) Schematic plot of the pore geometry

Fig. 5 Quantification of particle (or pore) orientation and pore shape

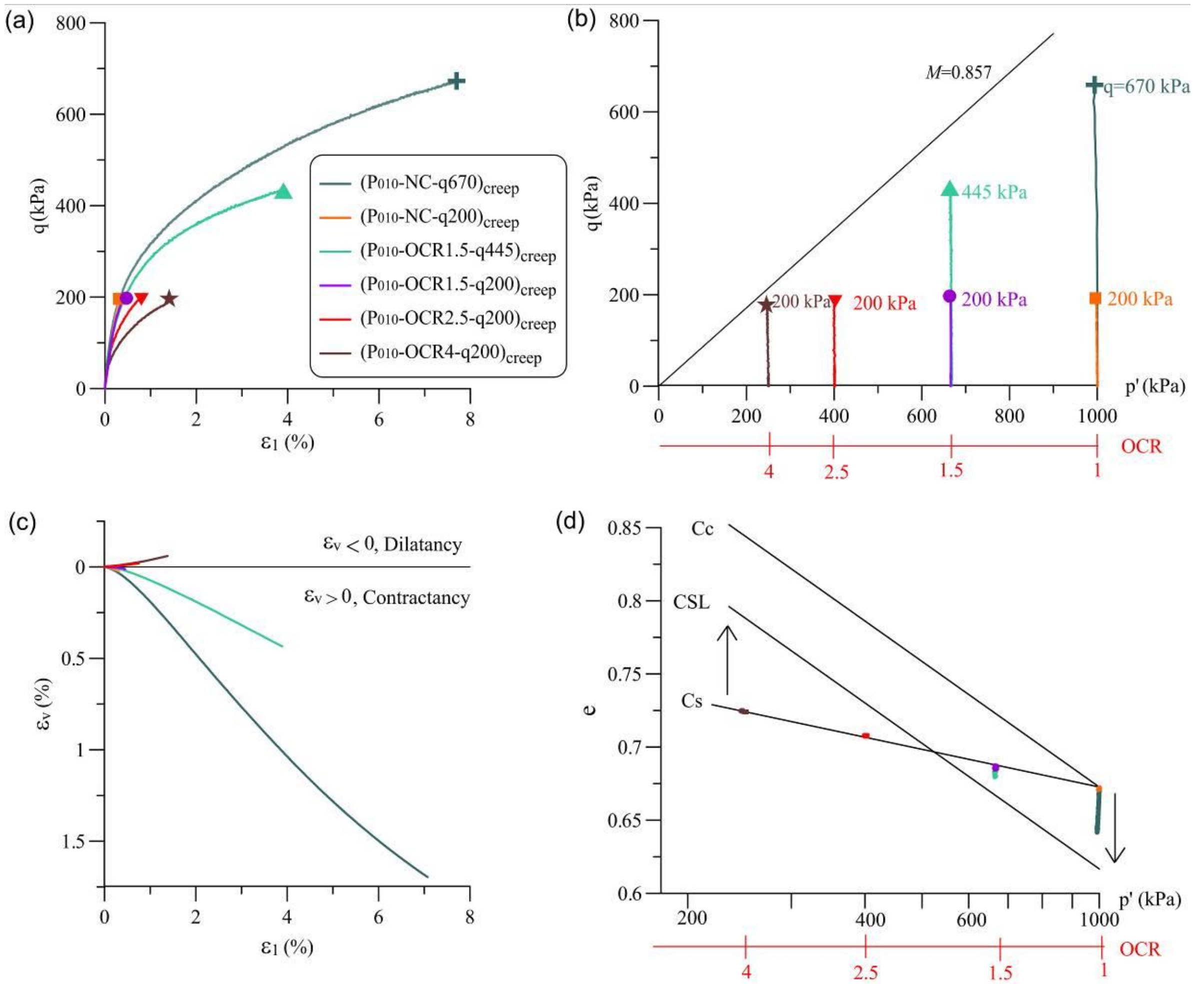

Fig. 6 Triaxial tests of test $(P_{010})_{creep}$ for Kaolin along *p*' constant stress paths

(a) (ε_1-q) plane; (b) (p'-q) plane; (c) (ε_1-ε_v) plane; (d) (log p'-e) plane

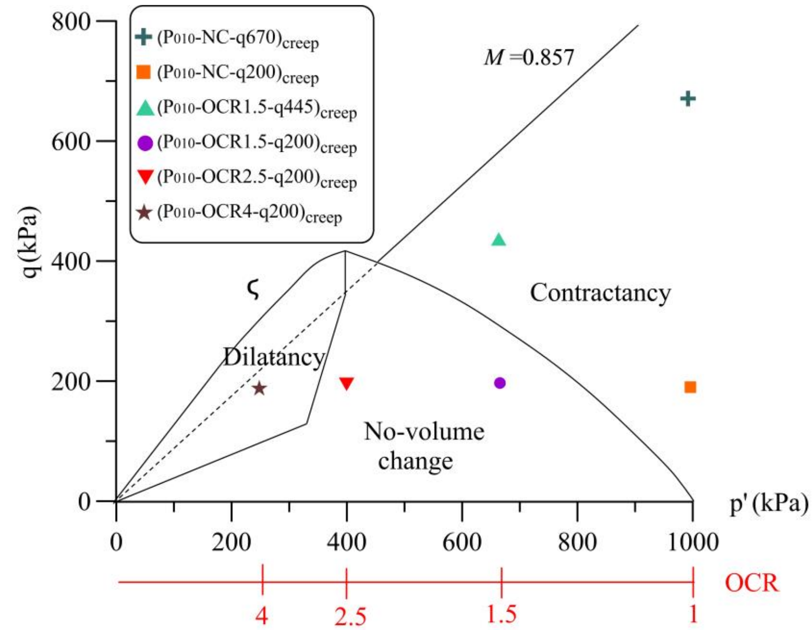

Fig. 7 Stress conditions in strain domains during pure creep phase

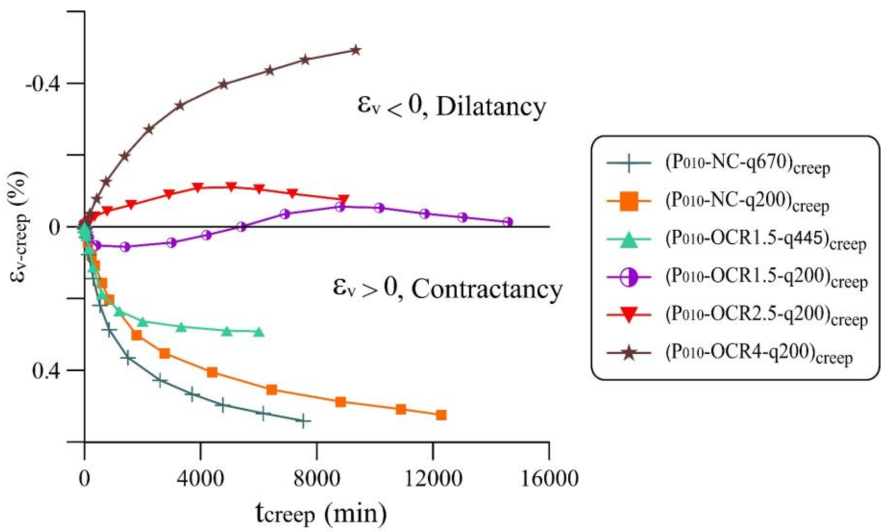

Fig. 8 Evolution of volumetric creep strain with time

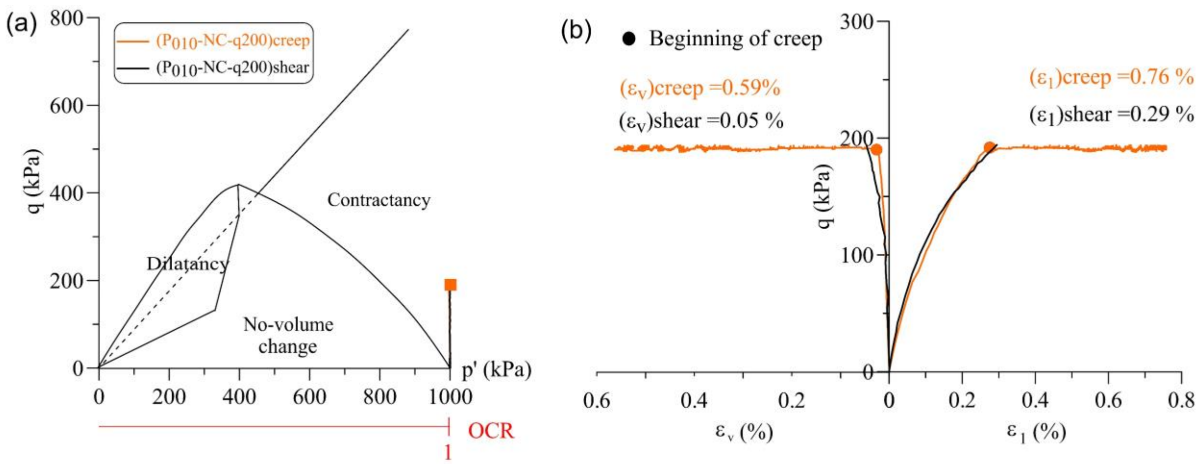

Fig. 9 Tests P_{010}-NC-q200 in contractancy domain: (a) in *(p′-q)* plane (b) strain evolution

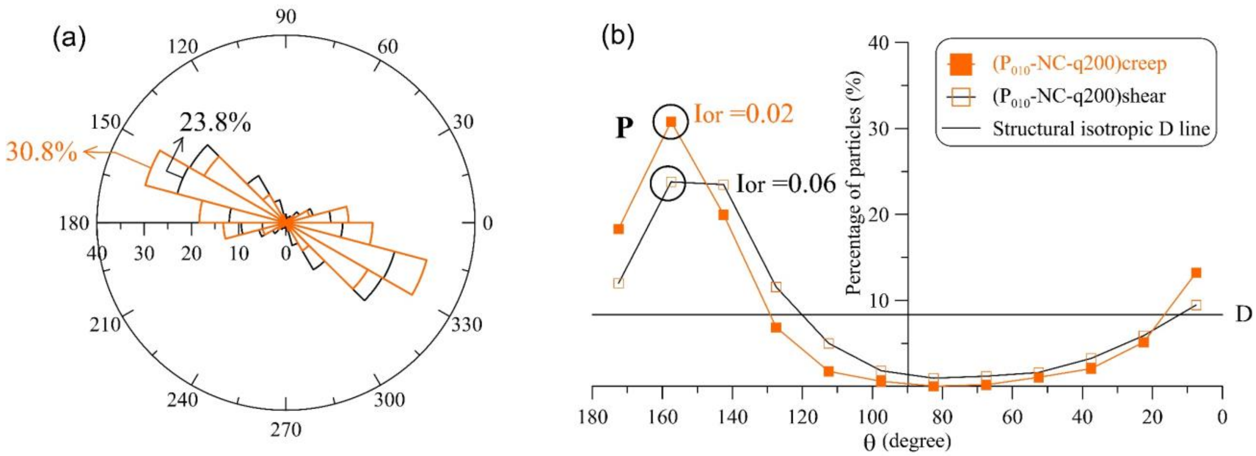

Fig. 10 Global particle orientation of specimens of Tests P_{010}-NC-q200:

(a) rose diagram; (b) orientation curve

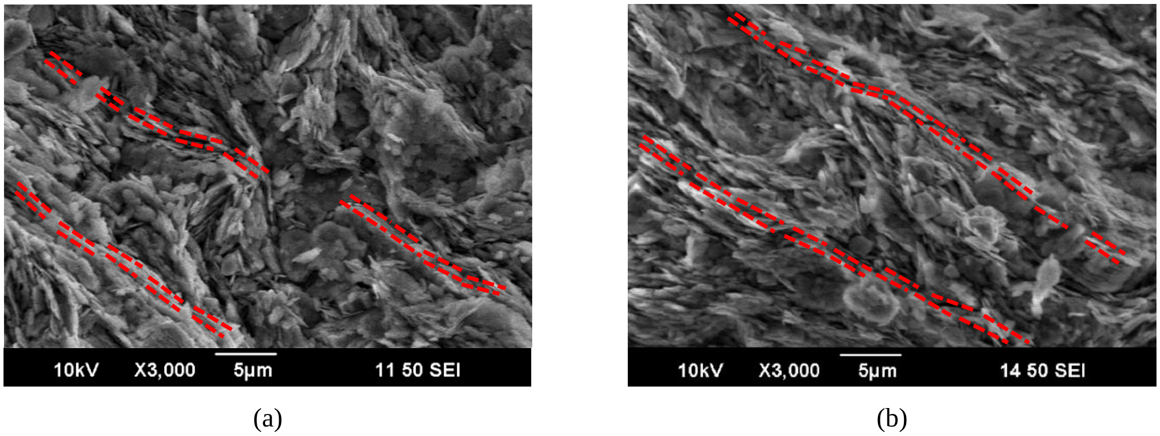

Fig. 11 Microfabric of tests P_{010}-NC-q200 in contractancy domain: (a) after shear (b) after creep

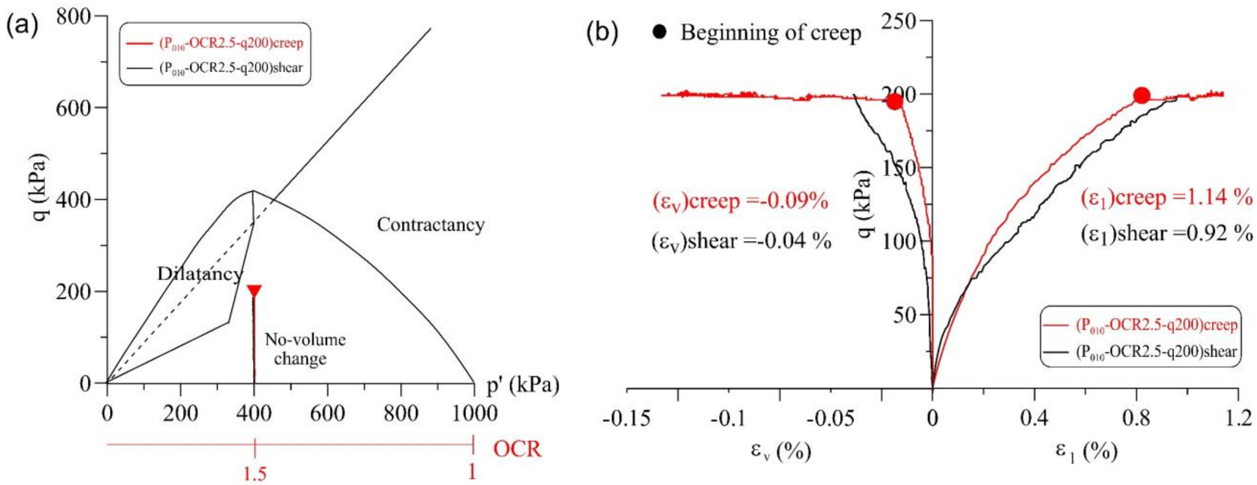

Fig. 12 Tests P_{010}-OCR2.5-q200 in pseudo-elastic domain: (a) in *(p'-q)* plane (b) strain evolution

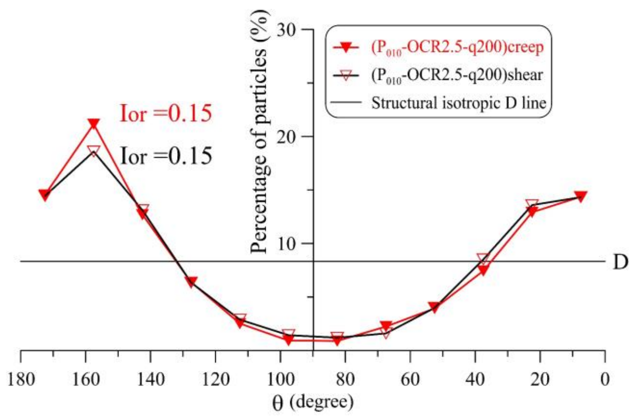

Fig. 13 Global particle orientation of specimens of tests P_{010}-OCR2.5-q200

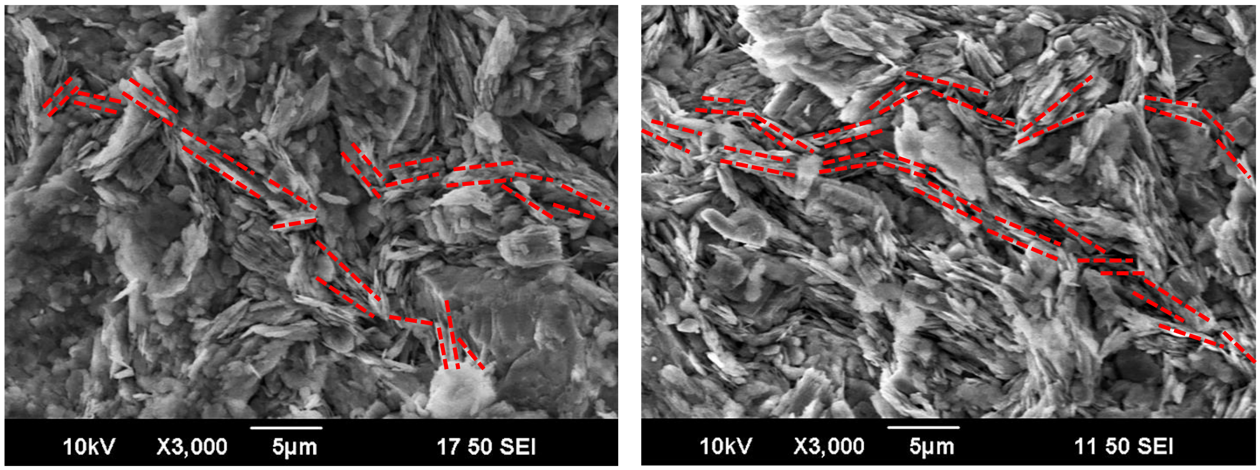

(a) (b)

Fig. 14 Microfabric of tests P_{010}-OCR2.5-q200 in pseudo-elastic domain: (a) after shear (b) after creep

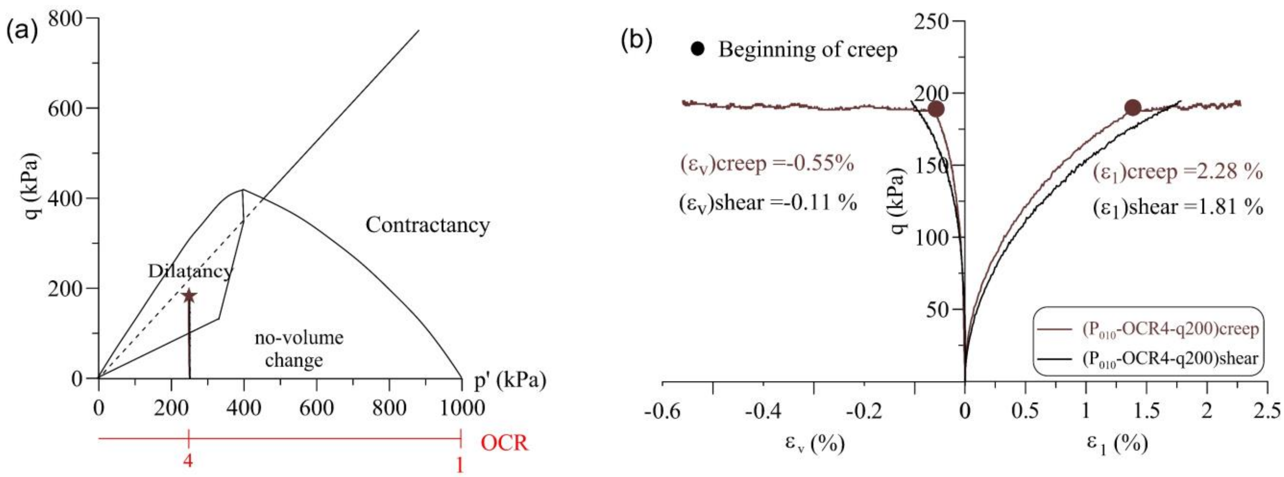

Fig. 15 Tests P_{010}-OCR4-q200 in dilatancy domain: (a) in *(p'-q)* plane (b) strain evolution

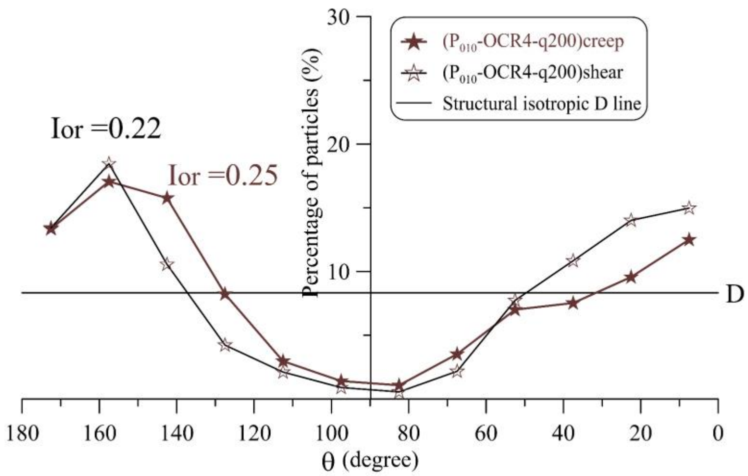

Fig. 16 Global particle orientation of specimens of tests P_{010}-OCR4-q200

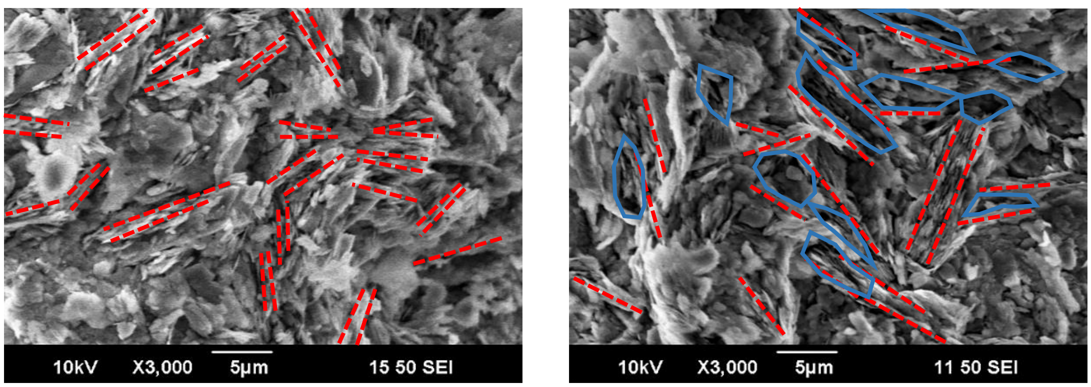

(a) (b)

Fig. 17 Microfabric of tests P_{010}-OCR4-q200 in dilatancy domain: (a) after shear (b) after creep

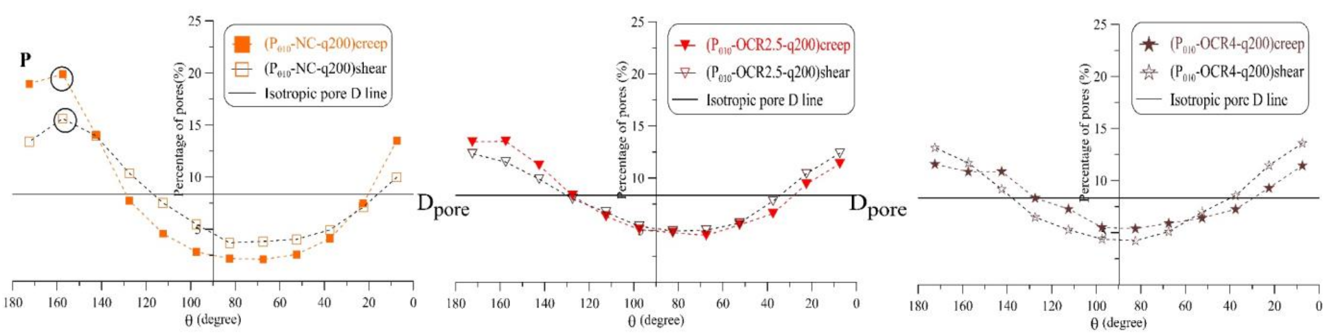

(a) (b) (c)

Fig. 18 Pore orientation of samples: (a) P_{010}-NC-q200 (b) P_{010}-OCR2.5-q200 (c) P_{010}-OCR4-q200

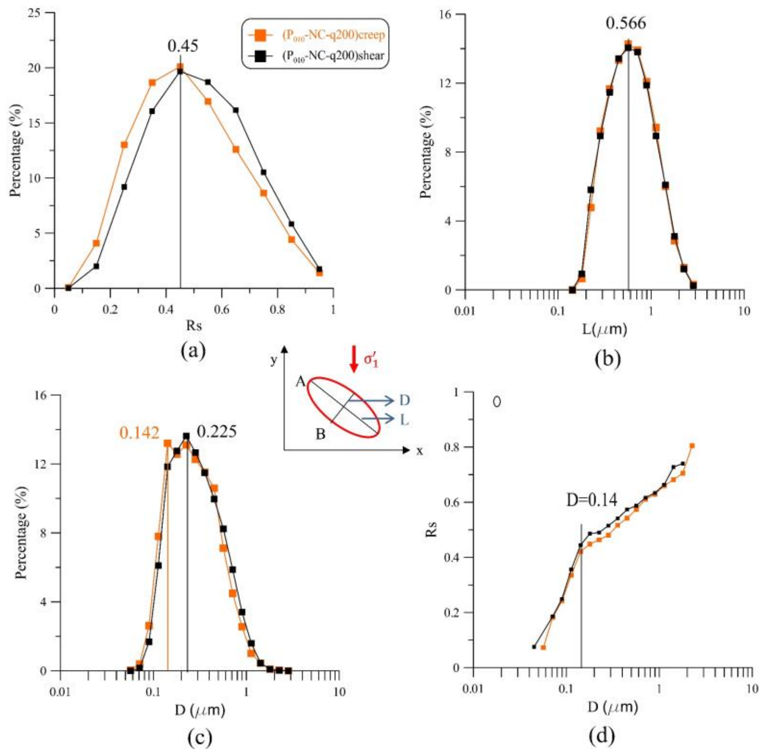

Fig. 19 Evolution of pore shape for tests P_{010}-NC-q200: (a) roundness (b) length (c) diameter (d) roundness vs diameter

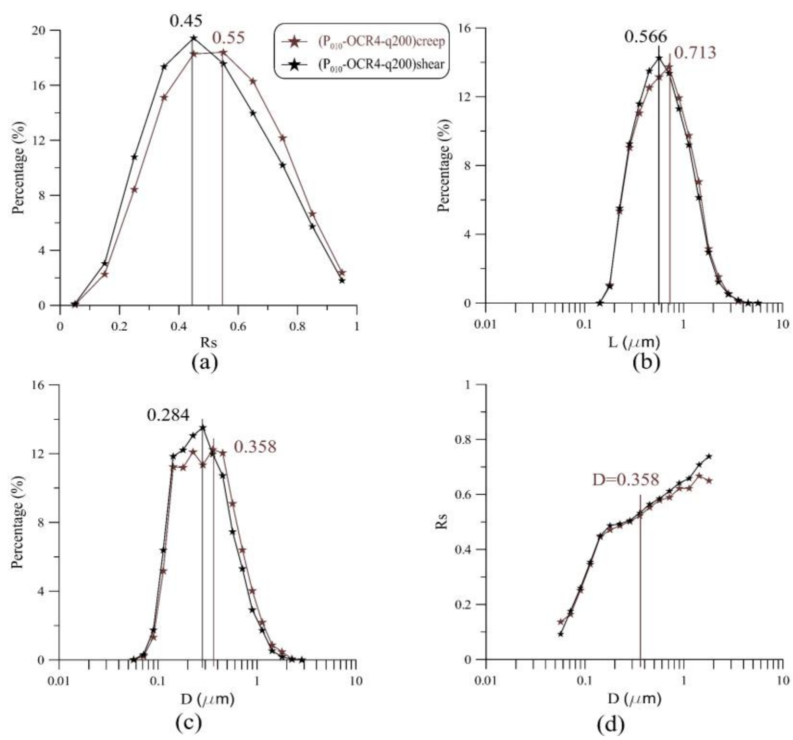

Fig. 20 Evolution of pore shape for tests P_{010}-OCR4-q200: (a) roundness (b) length (c) diameter (d) roundness vs diameter

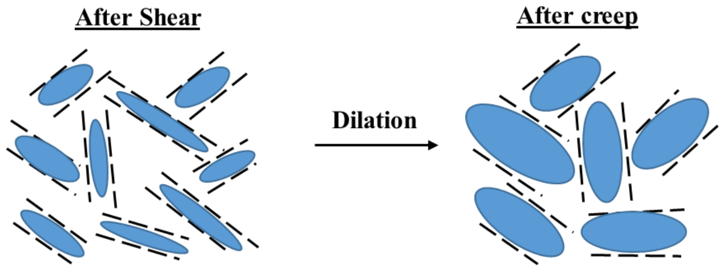

Fig. 21 Evolution of pores relates to creep dilation

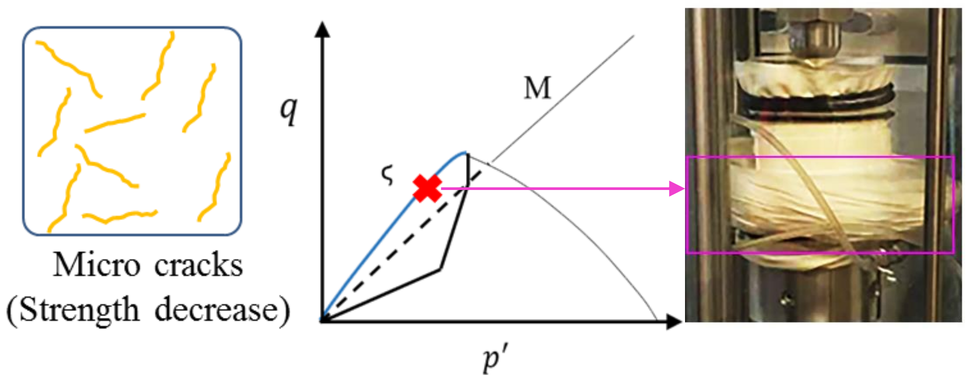

Fig. 22 Schematic diagram of creep collapse